RMetS
Royal Meteorological Society

Some considerations on the spectral features of meridional heat transport by transient eddies

G. Messori* and A. Czaja

Space and Atmospheric Physics Group, Department of Physics, Imperial College London, UK

*Correspondence to: G. Messori, Space and Atmospheric Physics Group, Department of Physics, Imperial College London, Room 714, Huxley Building, London, SW7 2AZ, UK. E-mail: gabriele.messori06@imperial.ac.uk

The present study analyses extreme events in meridional atmospheric heat transport due to transient eddies in the time–frequency domain. The data used are the European Centre for Medium-Range Weather Forecasts (ECMWF) ERA-Interim reanalysis data, at the 850 mb pressure level and with daily, 0.7° latitude and longitude resolution.

Fast-growing atmospheric modes are associated with large heat transport, which would suggest a link between transport extremes and growing baroclinic systems (defined here as motions in the 2.5–6 day band). However, by analyzing wavelet power spectra of transport extremes and of the corresponding meridional velocity and moist static energy temporal anomalies, this is found not to be the case. In fact, baroclinic systems provide only a modest contribution to the integrated power of the extreme heat transport event spectrum. The transport extremes are driven by very precise phase and coherence relationships between the velocity and moist static energy anomalies, acting over a broad range of frequencies (2.5–30 days). Planetary-scale motions ($k = 0$–4) with periods beyond 6 days play a key role in this framework.

Key Words: atmosphere; wavelet analysis; power spectrum; extreme event; phase; wave number

Received 27 March 2013; Revised 25 June 2013; Accepted 27 June 2013; Published online in Wiley Online Library 24 October 2013

1. Introduction

Transient motions drive a major portion of the poleward atmospheric heat transport in the mid-to-high latitudes (Peixoto and Oort, 1992). There is extensive literature on this topic, which has focused on both observational (e.g. Lau and Wallace, 1979) and theoretical (e.g. Branscome, 1983) considerations. A significant number of studies have also focused on time filters, in order to assess the time-scales driving transport variability. Blackmon *et al.* (1977) found that time-scales between 2.5 and 6 days and motions with periods beyond 10 days contributed to comparable portions of the transient-eddy heat transport, with the former dominating in the storm-track regions and the latter at higher latitudes. This vast literature has, however, largely overlooked the importance of extreme events in setting the seasonal mean transport by transient motions (with the notable exception of Swanson and Pierrehumbert, 1997). Indeed, the robust demonstration of this high sensitivity to extremes is very recent (Messori and Czaja, 2013, hereafter MC13).

In their study, MC13 found that just a very few days every season could account for over half of the net seasonal transport at a given location, in both winter and summer and Northern and Southern Hemispheres (NH and SH). Furthermore, these extreme occurrences displayed temporal and spatial scales compatible with phase-driven, baroclinic growing systems (Eady, 1949). However, the exact role of baroclinic time-scales in these systems was not quantified. Throughout this study, the term 'baroclinic time-scales' will be applied to periods between 2.5 and 6 days, following the terminology introduced by Blackmon *et al.*(1977).

While baroclinic motions might not be the single dominant component when considering the whole of the transport (e.g. Blackmon *et al.*, 1977), they would be expected to be the main drivers of extreme occurrences, in view of both the findings of MC13 and the intuitive link between extremes and growing systems. *A priori*, there is therefore no reason to doubt that the traditional view of growing systems as developing baroclinic disturbances should not apply to these extreme events.

Considering the transport as a product of anomalies in meridional velocity (v) and moist static energy (H, hereafter also referred to as MSE), one can apply the bandwidth theorem to test the plausibility of the argument. The theorem relates to any wave phenomenon and is commonly applied to wave packets. It relates the spread in frequencies ($\Delta\omega$) of the said phenomenon to its duration (Δt) via the inequality

$$\Delta t \Delta\omega \geq \frac{\pi}{2}. \quad (1)$$

This relation then suggests that baroclinic time-scales in v and H would constrain the transport signal duration according to

$$\Delta t \geq \frac{\pi}{2\Delta\omega}, \tag{2}$$

$$\Delta\omega = \frac{2\pi}{2.5 \text{ days}} - \frac{2\pi}{6 \text{ days}}, \tag{3}$$

corresponding to $\Delta t > 1$ day. MC13 have shown that heat transport extremes typically last for a few days. This lower bound therefore does not exclude baroclinic time-scales from driving extremes, but it is clearly inconclusive and implies that further analysis is needed.

The present study will show that the v and H anomalies leading to extreme events in heat transport are not predominantly linked to baroclinic time-scales. Moreover, the fractional contribution of these time-scales to the large heat transport occurring on extreme event days is found to be essentially indistinguishable from that seen on other days. After establishing robustly the role of longer time-scales in generating the extremes, we demonstrate that the key drivers are the phase and coherence relationships between the v and H anomalies. The structure of this article is as follows. Section 2 briefly describes the data and methodology utilized. Section 3 presents wavelet power spectra of the transport and highlights the role of phase and coherence. A physical interpretation of the extremes is also proposed. A discussion on the relevance of baroclinic time-scales and possible implications is given in section 4. Finally, section 5 offers conclusions and scope for further research.

2. Data and methodology

The present study utilizes the European Centre for Medium-Range Weather Forecasts (ECMWF) ERA-Interim reanalysis data (Simmons *et al.*, 2006). Similarly to MC13, 0.7° latitude and longitude resolution, daily (1200 UTC) fields at 850 mb are considered. The analysis includes 22 December, January and February (DJF) and 22 June, July and August (JJA) time series, from June 1989–February 2011.

The transient-eddy transport is computed as the product of v and H temporal anomalies (denoted by a prime). These are defined as departures from the quadratically detrended seasonal mean, and are computed between 30 and 89°N and 30 and 89°S. Velocity is positive polewards in both hemispheres. The analysis is performed over both land and ocean. For further details, the reader is referred to section 2 in MC13.

Extreme events are then chosen as values of $v'H'$ that exceed the 95th percentile of the distribution for the full hemisphere and time period considered. MC13 have shown that the exact percentile chosen as threshold does not affect the characteristics of the extremes. In order to avoid double-counting, in the case of several consecutive days at a given location exceeding the threshold only the local maximum of the $v'H'$ signal is retained. A Morlet wavelet transform is then applied to the selected $v'H'$ and the corresponding v' and H'. Note that the transform of the transport is computed as the transform of a single variable $v'H'$, not as the product of the transforms of v' and H'.

Wavelets are the optimal tool to analyse data in the time–frequency domain, allowing a detailed analysis of the signal's power throughout each extreme event. Furthermore, they also provide a time–frequency picture of phase and coherence of separate signals. These two features provide a complete overview of the frequency and phase relationships driving the extreme events, making wavelet transforms perfectly suited to the present spectral analysis. Similarly to more traditional Fourier transforms, however, wavelets do not yield significant results if applied to time series that are short compared to the time-scales being considered. In order to minimize this problem while avoiding adding data external to the seasons being considered, only the extreme events on the central day of every season are retained (i.e. 15 January and 16 July). While this criterion might seem excessively restrictive, it still provides around 4×10^4 events per season per hemisphere. As discussed below, this number is found to be sufficient to provide significant results. The wavelet power spectra for the selected events are then composited, so that a single spectrum for each signal is obtained for every season–hemisphere combination. For further details on the properties of the Morlet wavelet and on wavelet transforms in general, the reader is referred to Goupillaud *et al.* (1984), Torrence and Compo (1998) and Grinsted *et al.* (2004). Torrence and Compo have suggested that it is not good practice to composite wavelet spectra because the power maxima will be smeared out. Here we feel justified in adopting this approach because we are co-locating the extremes, where we expect the power to peak. To verify this further, the wavelet analysis was repeated in logarithmic space, computing the mean of the logarithm of the wavelet power and the standard deviation of the logarithm of the wavelet power. These quantities were then used to verify that the composite provides a good description of the typical extreme event, thus also indicating that a sufficient number of extremes have been selected.

Part of the analysis is also performed on time-filtered data. The filter used is a 21-point high-pass finite impulse response (FIR) filter, with a half-power cut-off at 8 days, and is designed to capture the full breadth of baroclinic time-scales. Even though our definition of these time-scales considers a more restrictive interval, Chang (1993) suggested that filters with a 6 day cut-off lose a key part of the baroclinic variance. Here, we therefore follow Nakamura *et al.* (2002) in choosing an 8 day cut-off so as to retain the full variability in the 2.5–6 day band. The filter can be tested by computing the spectral power of the filtered and unfiltered v' and H' signals in the 2–6 day range. It is found that typically less than 5% of the power is lost when the filter is applied. Further details are provided in section 3.1.

The present paper also analyses wave-number power spectra. To obtain them, the v', H' and $v'H'$ signals around a given latitude circle, for all days of a given season, are decomposed into single wave-number contributions using a fast Fourier transform algorithm. This yields one coefficient per day per wave number. A Fourier amplitude spectrum is then computed in the time domain for each wave number, yielding spectral power versus period (or frequency). This procedure is repeated for all latitudes and years considered. Finally, the spectra thus obtained are composited, yielding a single spectrum for every season–hemisphere combination.

To verify that none of the results presented below depends on artefacts of the statistical analysis performed, a number of verifications were carried out. As a first step, the whole analysis was repeated using non-detrended data. Next, the wavelet transforms were repeated using a Paul wavelet. To test the robustness of the wavelet analysis further, the period-averaged wavelet spectra were compared with the traditional Fourier spectra. Finally, the filtering was repeated using the band-pass filter from Blackmon and Lau (1980). None of these changes affected the qualitative aspects of the results presented in this study.

3. Wavelet spectra of extreme heat transport events

3.1. *General features of the power spectra*

To investigate the spectra of transient-eddy heat transport extremes, we begin by computing a composite power spectrum,

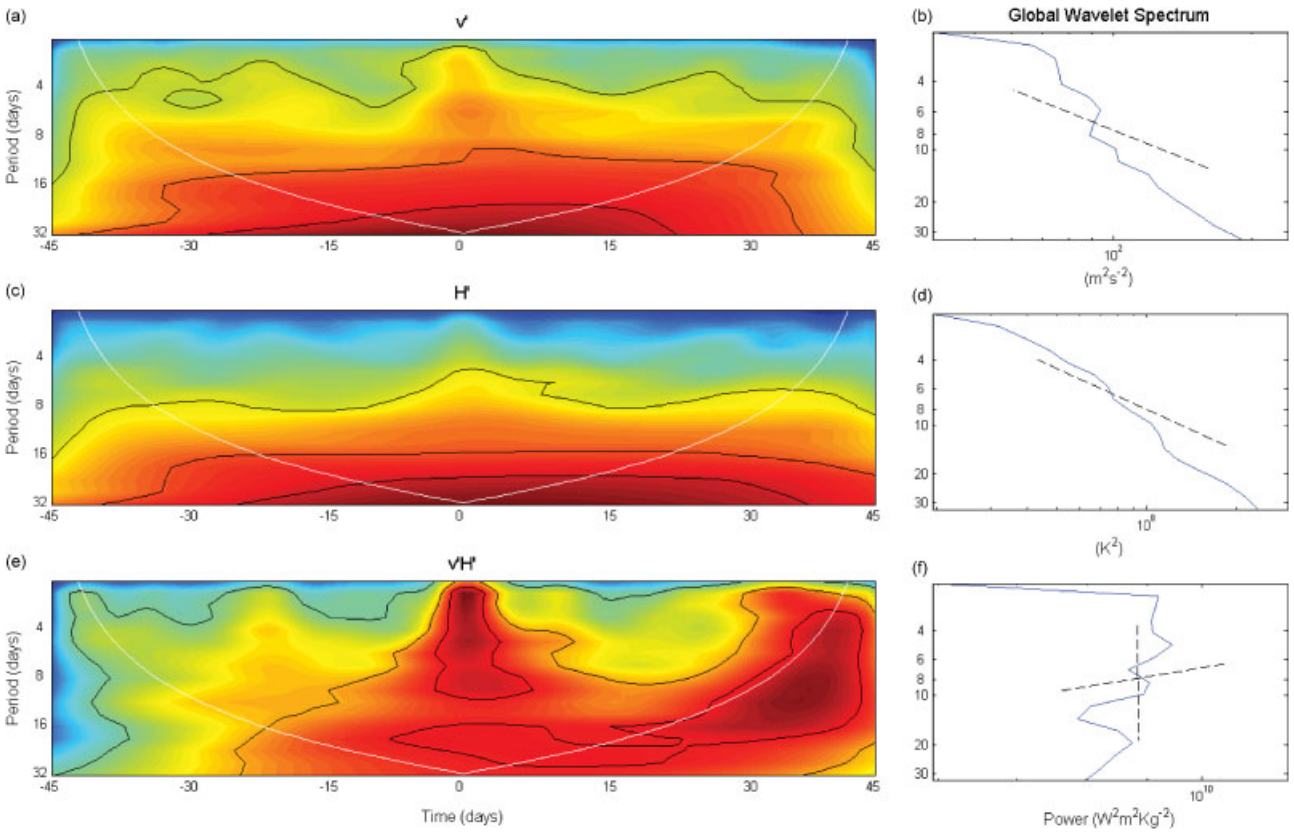

Figure 1. Composite wavelet power spectra of (a) meridional velocity anomalies, (c) moist static energy anomalies and (e) atmospheric heat transport due to transient eddies. The spectra are centred on local maxima of transport extreme events. Negative times correspond to days before the extremes, positive ones to days following them. Darker shades indicate higher values. The white contours represent the cone of influence. Panels (b), (d) and (f) display the corresponding time-averaged spectra, for the five days centred on the extremes, on a log–log scale. The dashed lines in (b) and (d) are reference positive unit slopes. Those in (f) have slopes 0 and −1 respectively. The data cover NH DJFs from December 1989–February 2011. This figure is available in colour online at wileyonlinelibrary.com/journal/qj

taking into consideration all available NH latitude bands (30–89°N) and DJF time series (1989/1990–2010/2011). Figure 1 shows the composite power spectra for v', H' and $v'H'$ (panels (a), (c) and (e) respectively). It should be noted that the latter spectrum was computed by treating the transport as a single variable, as described in section 2. The white contours indicate the cones of influence, which represent the limit beyond which edge effects become important. Only the data above these lines should therefore be considered. Darker shades indicate higher spectral power. Also displayed are the time-averaged spectra for the five days centred on the extreme event and reference slopes (panels (b), (d) and (f) respectively). The five-day window was chosen to ensure that the full breadth of the extremes was captured, following the durations found by MC13. The key features of the spectra are (i) a clear increase in power with increasing period in v' and H' and (ii) an approximately flat power spectrum in $v'H'$, with a modest peak at periods around 3–5 days. The latter feature is consistent with the typical extreme event duration of 2–7 days reported in MC13. The differences between the spectra are illustrated very clearly in Figure 1(b), (d) and (f). The dashed lines in (b) and (d) are reference positive unit slopes, while the ones in (f) are zero and negative unit slopes respectively, highlighting the flatness of the spectrum. Similar observations apply to the corresponding SH JJA time series, shown in Figure 2, although here the $v'H'$ spectrum is slightly more tilted than in Figure 1. Another notable feature of the $v'H'$ spectra is the asymmetry in the power before and after the event. This is very marked in Figure 1(e), while it is much less pronounced in Figure 2(e). While a large part of the said asymmetry occurs within the cone of influence of the wavelet, the shorter periods also display it clearly. This could be linked to the spatial structure of the extreme events and will be discussed further in Section 4.

The discrepancy between the $v'H'$ power spectrum and those of v' and H', suggests that there must be a systematic interaction pattern between v' and H' driving the 'flattening' of the transport spectrum. Furthermore, since transport is the result of a product of two signals and the wavelet transform is computed on the product, a scaling factor must be taken into account. So, for example, periods of 10 days in v' and H' potentially could affect the five-day band in $v'H'$. This suggests that a broad range of frequencies, beyond the 2.5–6 day range, might be contributing to this 'flattening' effect.

To investigate these contributions in greater detail, the v' and H' data are high-pass filtered (periods < 8 days) using the filter described in section 2. The filter cut-off period is well beyond that of our range of interest, to ensure that power loss due to filter design is minimized. A composite power spectrum is produced following the same procedure as for the unfiltered data (see Section 2). Next, the power in the wavelet spectrum in the five days centred on the extreme event is summed over all periods within the cone of influence. Last, a ratio between the summed power of the filtered and unfiltered data is computed. In taking the ratio, the same range of periods is included in both the filtered and unfiltered integrals, even where these fall well outside the baroclinic range. This ensures that the full breadth of contributions by the baroclinic-scale v' and H' motions is captured. Depending on the hemisphere–season combination, it is found that the power spectrum resulting from the filtered data captures between 22 and 35% of the power found in the original spectrum (Table 1(a)). If one replicates the analysis selecting events within 5 percentiles of the median of the poleward-only

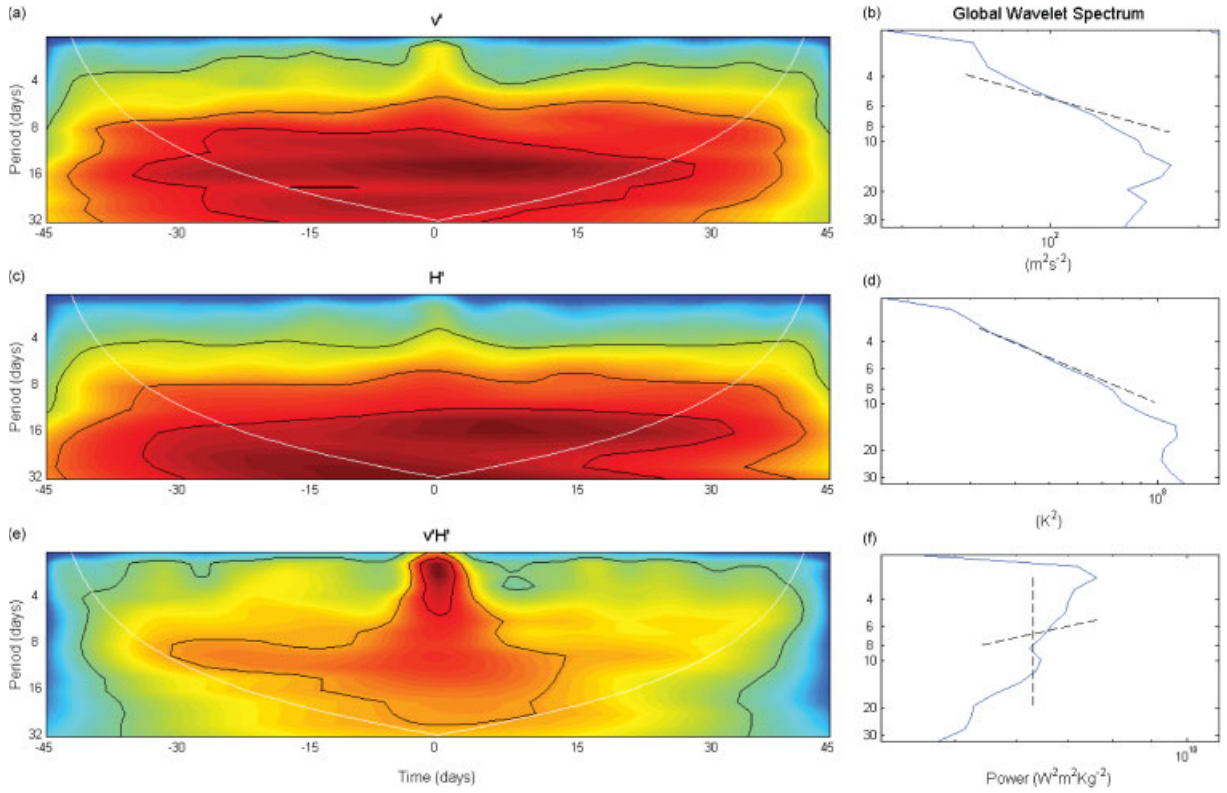

Figure 2. Same as Figure 1, but for SH JJAs from June 1989–August 2010. This figure is available in colour online at wileyonlinelibrary.com/journal/qj

Table 1. Fractional contribution of baroclinic v' and H' fluctuations to the period-integrated $v'H'$ power spectrum over a 5 day window centred on events in (a) the top 5 percentiles of the $v'H'$ distribution and (b) within 5 percentiles of the median value of the poleward-only distribution. The data cover all of the 44 seasons considered (June 1989–February 2011).

Event	Hemisphere	Season	Ratio
(a) Extreme	N	DJF	0.31
		JJA	0.22
	S	DJF	0.35
		JJA	0.31
(b) Median	N	DJF	0.24
		JJA	0.18
	S	DJF	0.36
		JJA	0.33

heat transport distribution, rather than extreme events, the ratios are very similar, with only a modest difference emerging during the NH winter (Table 1(b)).

The contribution from baroclinic periods in v' and H' is therefore comparable for extreme and median events. In both cases, these time-scales do not drive the bulk of the transport, which must therefore come from longer periods.

To test this hypothesis further, time-averaged wavelet spectra, similar to those in Figures 1(b), (d) and (f) and 2(b), (d) and (f), are computed for the filtered signals. Figure 3 displays the time-averaged wavelet spectra for the 5 days centred on the extreme event, for both the filtered (continuous line) and unfiltered (dashed line) signals. Panels (a), (c) and (e) display the spectra for v', H' and $v'H'$ respectively, during NH DJF. Panels (b), (d) and (f) display the corresponding spectra for SH JJA. It should be noted that the filtered spectra in (e) and (f) are not the spectra of the filtered $v'H'$ signal but rather the spectra of the $v'H'$ signal resulting from the product of the filtered v' and H' ones. The dotted lines mark the limit of baroclinic time-scales. The numbers in the top left-hand corner of the panels are the ratios between the period-integrated powers of the filtered and unfiltered signals in the 2–6 day range only. The key features of the figure are as follows: (i) the very small loss in power of the v' and H' signals at periods below 6 days; (ii) the large loss in power of the $v'H'$ signal in the same range; and (iii) non-zero power at periods beyond 6 days, always in the $v'H'$ signal. The first feature, combined with the ratios shown in the panels, demonstrates that the filter's design has a reduced impact on the v' and H' signals at baroclinic time-scales. The reduction in power of the $v'H'$ spectrum below 6 days confirms the limited role of these periods and implies that the longer periods in v' and H', suppressed by the filter, must play a large role in driving shorter scale fluctuations in the $v'H'$ signal. Last, it should not be surprising that the $v'H'$ signal displays non-zero power at periods beyond the filter cut-off, because of the complex interplay of different frequencies driving the transport. A similar behaviour can be easily tested by substituting the atmospheric data analysed here for a simple superposition of sinusoidal signals.

3.2. *The role of phase and coherence*

The velocity and MSE fluctuations do not display a clear peak at baroclinic scales, as seen in the spectra in Figure 1, and cross-power spectra of v' and H' (not shown) confirm that most of the power the two signals share resides at long periods, well above baroclinic time-scales. The shift towards higher frequencies seen in the $v'H'$ spectrum can only be explained by a systematic phase and coherence relationship between v' and H' perturbations. Figure 4 shows the composite coherence–phase plot for NH DJF transport extremes; Figure 5 shows the corresponding plot for SH JJA. Figure 4(a) depicts coherence as colours and phase as arrows. The black contour indicates the cone of influence, which represents the limit beyond which edge effects become important. As in Figure 1, only the data above this line should be considered. Since phase for incoherent signals has no meaning, phase arrows are only retained in regions where coherence is

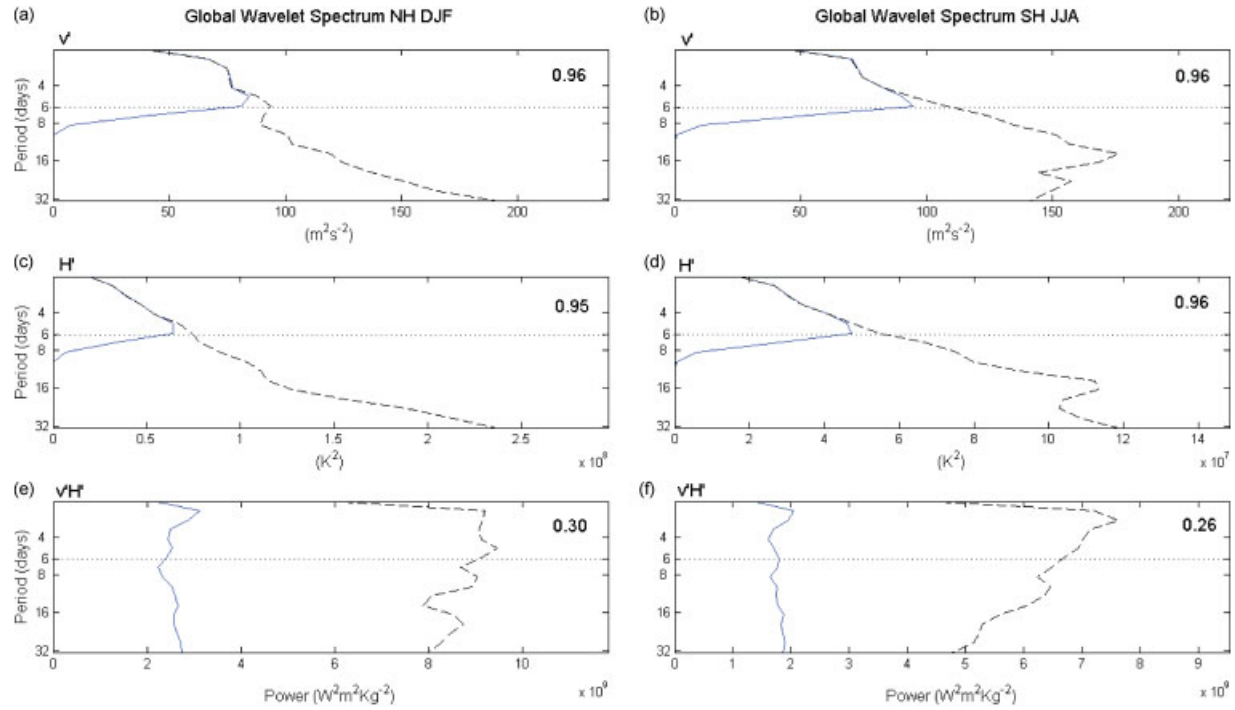

Figure 3. Global (time-averaged) wavelet spectra for v', H' and $v'H'$ during NH DJF (panels (a), (c) and (d) respectively) and SH JJA (panels (b), (d) and (f) respectively). The time span considered covers the five days centred on the extremes. The continuous lines are the spectra of the filtered v' and H' and the resulting $v'H'$. The dashed lines are the spectra of the unfiltered signals. The dotted lines mark the limit of baroclinic time-scales (2.5–6 days). The numbers in the top left-hand corner of the panels are the ratios between the period-integrated powers of the filtered and unfiltered signals in the baroclinic range. The data cover NH DJFs from December 1989–February 2011 and SH JJAs from June 1989–August 2010. This figure is available in colour online at wileyonlinelibrary.com/journal/qj

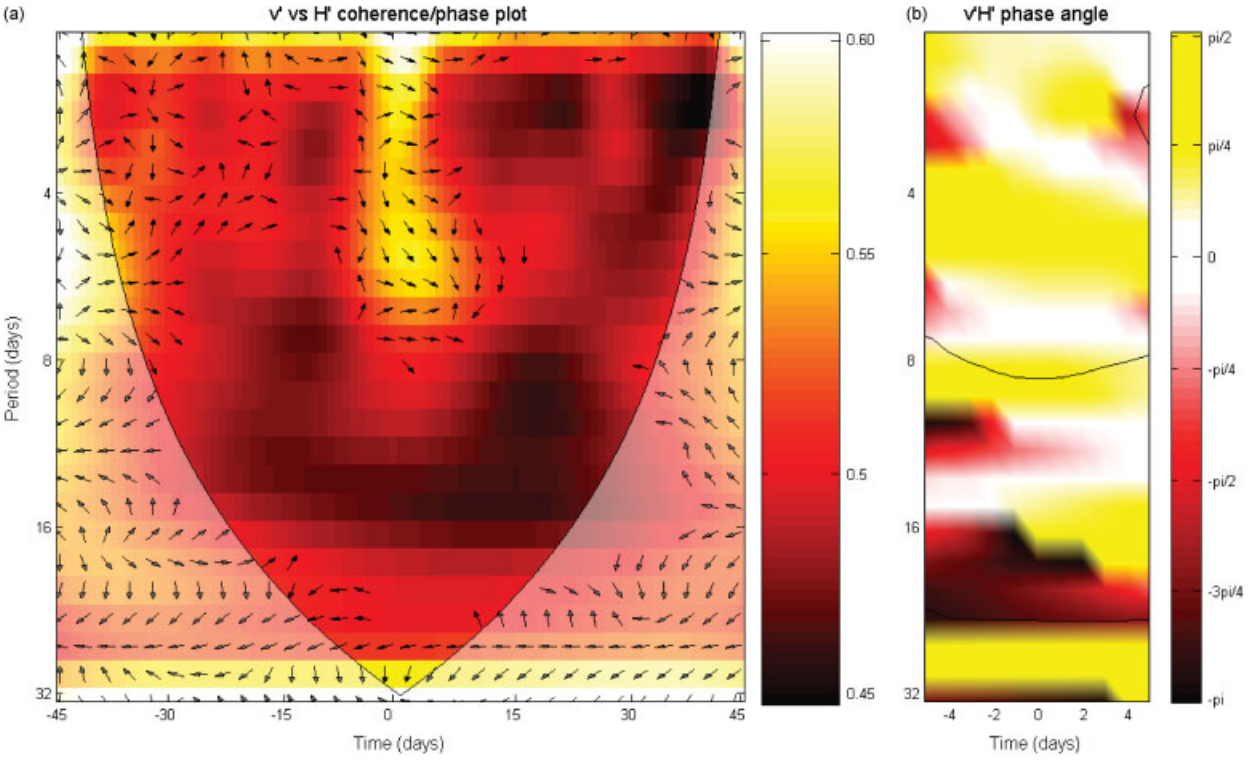

Figure 4. (a) Composite wavelet coherence/phase spectrum for meridional velocity and moist static energy anomalies. The spectra are centred on local maxima of transport extreme events. The colour map represents coherence values, the arrows the phase relationship. When the arrows point right, the v' and H' signals are perfectly in phase; when they point upwards, the two signals are in quadrature with v' leading H'. The converse holds for leftward and downward-pointing arrows. The black contour represents the cone of influence. (b) Phase angle in colour for the ten days centred on the extreme events. The scale is in radians. Again, positive values indicate that velocity leads MSE; the black contours bound the regions where coherence exceeds 0.5. The data range is the same as in Figure 1. This figure is available in colour online at wileyonlinelibrary.com/journal/qj

greater than 0.5. When the arrows point right, the v' and H' signals are perfectly in phase; when they point upwards the two signals are in quadrature, with v' leading H'. The converse holds for leftward and downward-pointing arrows. Figure 4(b) depicts the phase angle in colours for the 10 days centred on the extreme events. Again, positive values indicate that velocity leads MSE; the black contours bound the regions where coherence exceeds 0.5.

For the NH, three features emerge to explain the patterns seen in Figure 1: (i) the coherence is highest at periods of approximately 2–8 days; (ii) the phase angle is smallest at

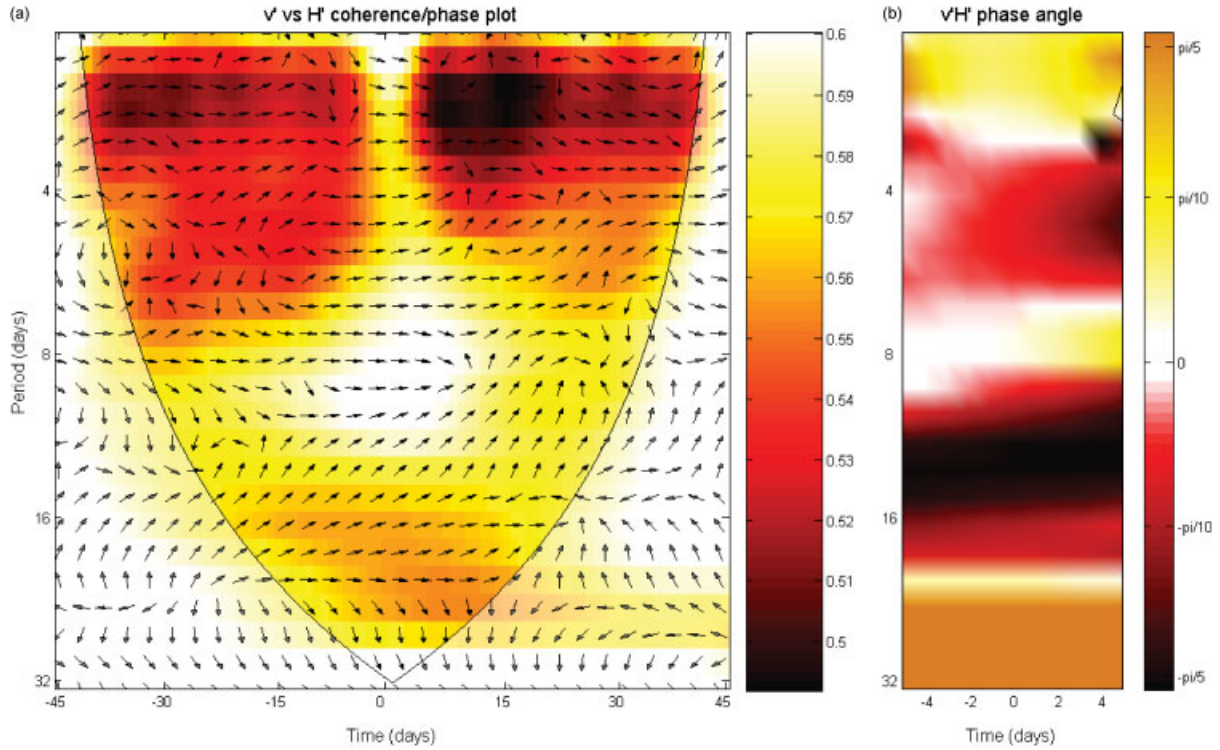

Figure 5. Same as Figure 4, but for SH JJA from June 1989–August 2010. This figure is available in colour online at wileyonlinelibrary.com/journal/qj

approximately 3–7 days; and (iii) at longer periods, v' and H' approach either quadrature or anti-phase. Similar considerations, albeit with slightly different numbers, can be made for the SH (Figure 5). At all but the lowest frequencies the phase angle stays relatively small, while the coherence values are systematically higher than those seen in the NH. Nonetheless, there is still a clear peak in coherence, now shifted more towards the 6–12 day range, and the phase angle is smallest at 2–3 and 7–8 days. The 'flattening' in the $v'H'$ spectrum is therefore driven by coherent, in-phase v' and H' disturbances*, while the unfavourable phase relationship at higher periods masks the high power of the two signals there. If not for this 'braking' role of phase, there would therefore be significantly more power at long periods in the $v'H'$ spectrum. This effect is evident in both hemispheres, while the differences in coherence between the SH and NH lead to more subtle considerations and will be discussed further in section 3.3.

It is interesting to note that, in both Figures 4 and 5, the data seem to display phase angles smaller than the Eady angle (which is approximately 21°). The latter is the theoretical lower bound on the phase angle of the velocity and temperature components of baroclinic disturbances. The Eady model, however, considers a highly idealized set-up of monochromatic, coherent waves, so it is not obvious that the numerical limits it sets should be obeyed exactly by real-world instabilities.

To illustrate further the importance of phase and coherence, composite wavelet spectra for a set of random events were computed (see Figure 6). These are data selected at random locations, on the same days and over the same range of latitudes and longitudes as the extreme events, for NH DJF. A number of data points similar to the number of extreme events were chosen and the spectra were then composited, exactly as for the extremes. The v' and H' spectra are comparable to those seen in Figure 1(a) and (c), while the $v'H'$ spectrum is extremely different from that in Figure 1(e) and is, in fact, very similar to the velocity and MSE ones. The distinctive feature of extreme events therefore does not lie in the power spectrum of the v' and H' fluctuations, but in their phase and coherence relationship. As might intuitively be expected, both aspects are essential. Indeed, an artificial $v'H'$ spectrum (not shown) was reconstructed using the actual coherence of the v' and H' signals, but applying a random phase at all periods, and none of the patterns discussed above was reproduced. Therefore neither coherence nor, obviously, phase alone can explain the $v'H'$ spectrum.

Maps analogous to those in Figures 1–5 have been computed for the remaining seasons and hemispheres (not shown). While the magnitude of the spectra, the coherence and the phase angles show some seasonality, the qualitative features identified above are robust characteristics of the data analysed.

3.3. *Inter-hemispheric differences*

The spectra of the different seasons and hemispheres present a coherent picture and share the same qualitative results. It should, however, be noted that the coherence values in NH JJA are, perhaps, too small to allow us to make definitive statements using phase, while coherence values in the SH are generally larger. This is evident by comparing Figures 4(a) and 5(a) and a similar pattern emerges when comparing NH JJA with SH DJF. A possible explanation could be related to the different storm track configurations in the two hemispheres, with the SH storm track being more extensive than its NH counterpart. Since a high coherence can be expected in these areas of strong growth, this difference could drive the higher coherence values found in the SH. To the authors' knowledge, however, no references or conclusive explanations for this difference exist in the literature.

These differences in coherence between the two hemispheres drive some interesting mechanisms. Systematically higher coherence values mean that phase angles at all periods have

*Note that, since heat transport results from the product of v' and H', a scaling factor in frequency (and therefore in period) must be taken into account here.

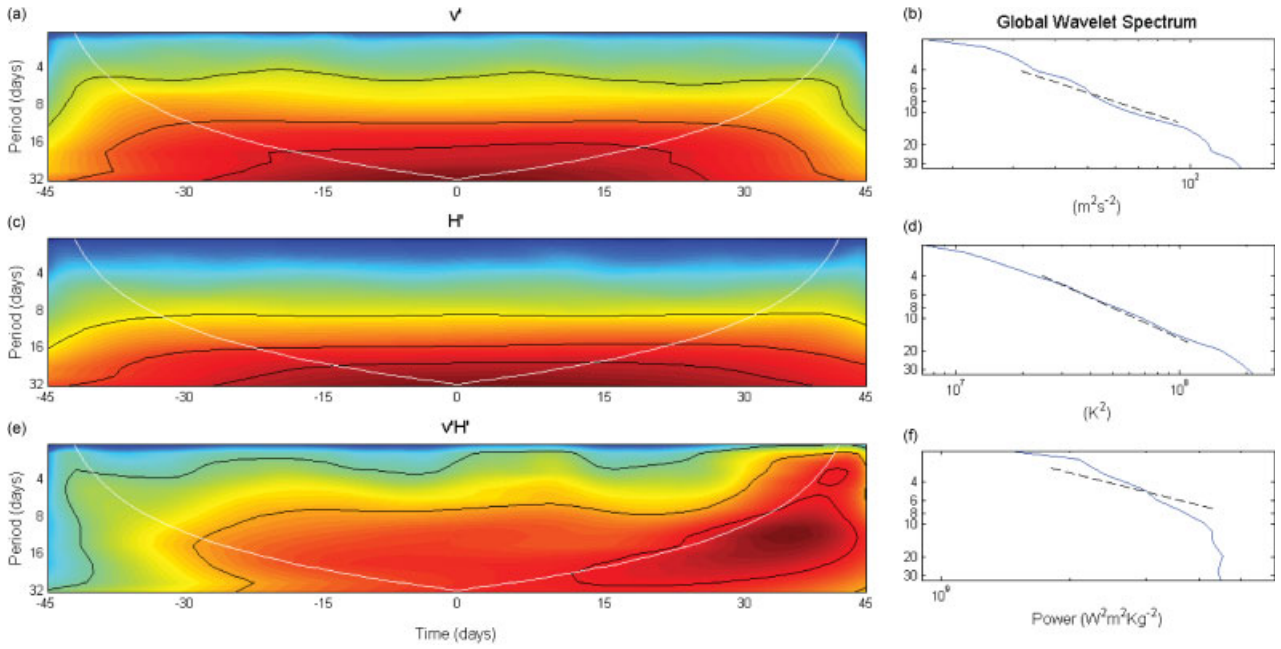

Figure 6. Same as Figure 1, but for heat transport events selected at random locations, on the same days and over the same range of latitude and longitude as the extreme events. Unlike in Figures 1 and 2, the dashed line in (f) also has positive unit slope. This figure is available in colour online at wileyonlinelibrary.com/journal/qj

a strong impact on the resulting $v'H'$ spectrum. In the SH, coherence therefore has a comparatively less important role than in the NH. As a *gedanken* experiment, consider the situation in which velocity and MSE have, throughout their full range of frequencies, the same phase angle. Assume further that this angle happens to be the optimal one for transporting heat; in the spirit of this idealized set up, this is taken to be the angle found in the Eady model of baroclinic instability (21°). If this is imposed on the actual coherence found, it will result in a 'flattening' of the $v'H'$ spectrum in the NH but not in the SH (not shown). In the NH, where coherence is generally low, the phase angle only has an effect at periods where coherence is higher than average. These happen to be within the baroclinic range, as discussed above. In the SH, where coherence is high at all periods, phase becomes instrumental in directing the power in the $v'H'$ spectra, meaning that imposing an Eady phase at all periods leads to the loss of the 'flattening' effect seen in the real data.

3.4. *Physical interpretation*

The secondary contribution of baroclinic time-scales to the $v'H'$ power spectrum, discussed in section 3.1, highlights the key role played by longer periods. These can be related to physical analogues in the atmosphere by investigating the spatial scales driving the transport. In order to do this, the power in the v', H' and $v'H'$ signals is decomposed into single wave-number contributions (hereafter also referred to as k), following the procedure described in section 2. All available NH latitude bands (30–89°N) and DJF time series (1989/1990–2010/2011) are taken into consideration. A caveat of this technique is that, since it takes into account full latitude circles, it is not limited to the locations of extreme events. Figure 7 shows the composite power spectra for v', H' and $v'H'$ (panels (a), (c) and (e) respectively) for wave number as a function of period. Darker shades indicate higher spectral power. Also displayed are the period-averaged spectra for the 10–32 day range (panels (b), (d) and (f) respectively). These are normalized relative to the spectral peak, so that the contribution of each wave number is expressed as a dimensionless fraction of the contribution from the dominating wave number. The lower bound of the integration range was set to 10 days to ensure that it was well beyond the range of the filter used in section 3.1, which has its half-power cut-off at 8 days. The upper bound was chosen to coincide with the longest periods resolved by the wavelet spectra discussed above. From Figure 7, it is immediately clear that planetary-scale waves ($k \leq 4$) dominate the spectrum. The peak contributions in the v', H' and $v'H'$ spectra come from $k = 3$–4, $k = 0$ and $k = 1$ respectively. Similar considerations apply to the NH JJA season (not shown). The corresponding plot for SH JJA (Figure 8) again shows similar results, with the peaks for the v', H' and $v'H'$ spectra now being respectively $k = 4$, $k = 0$, 3–4 and $k = 0$. The SH DJF season (not shown) differs slightly from the above in that the transport spectrum peaks at $k = 4$. The latter spectrum reproduces the corresponding v' spectrum quite closely and could be related to the typical $k = 4$–7 patterns seen in the SH summertime circulation (e.g. Hamilton, 1983).

As already mentioned, the results discussed above refer to an analysis of full latitude circles and are not limited to the locations of extreme events. Nevertheless, they can provide important insights into the origin of the low frequencies in the power spectra of extremes. Indeed, there is no reason to suspect that the motions accounting for low frequencies in the extreme events are distinct from those driving the same frequencies in the full latitudinal data. The power lost in applying the baroclinic filter to v' and H', namely that due to motions with periods beyond 8 days, therefore comes primarily from very low wave numbers in the range $0 \leq k \leq 4$. Similarly low wave numbers account for the majority of the transport's spectral power at long periods. Allowing for the significant seasonal and inter-hemispheric differences found, we interpret these results as indicating that the power seen in the $v'H'$ wavelet transforms at long periods is driven by planetary-scale waves. This suggests that extreme events in meridional heat transport by transient eddies are not merely the signatures of passing synoptic systems, but are driven by larger-scale modes of atmospheric variability. This is a novel result in the context of extreme events and is consistent with the known influence of large-scale modes, such as the North Atlantic Oscillation, on meridional eddy heat transport (e.g. Carleton, 1988).

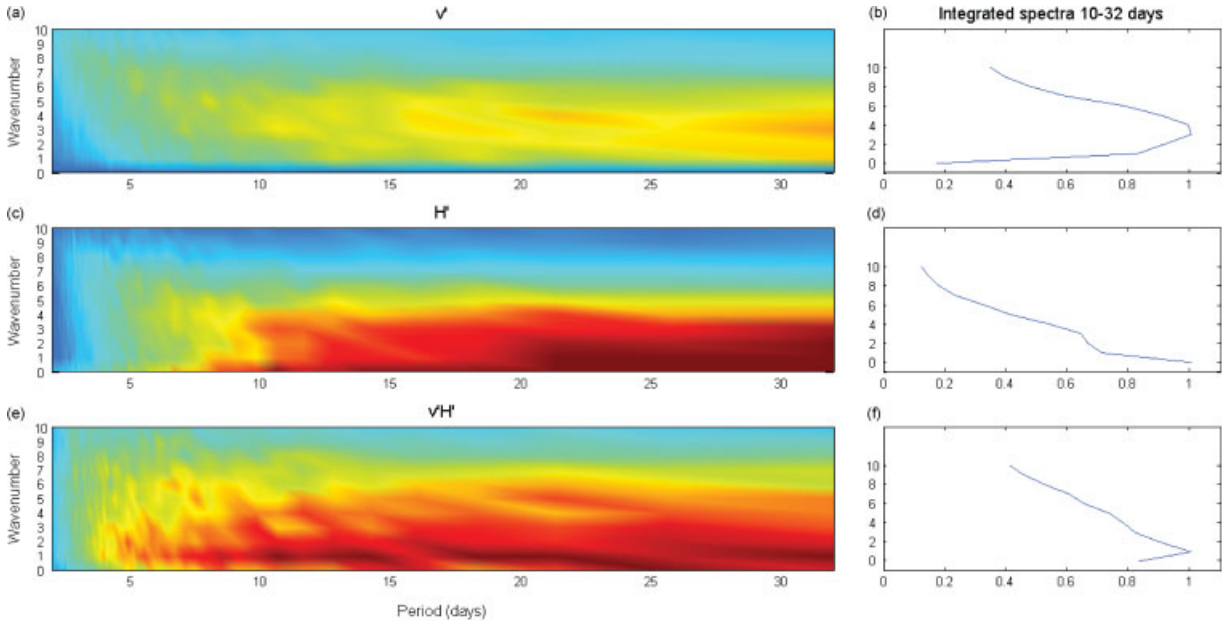

Figure 7. Composite Fourier power spectra of (a) meridional velocity anomalies, (c) moist static energy anomalies and (e) atmospheric heat transport due to transient eddies. The spectra are a function of wave number versus period. Darker colours indicate higher values. Panels (b), (d) and (f) display the corresponding spectra averaged over the range 10–32 days. The data range is the same as in Figure 1. This figure is available in colour online at wileyonlinelibrary.com/journal/qj

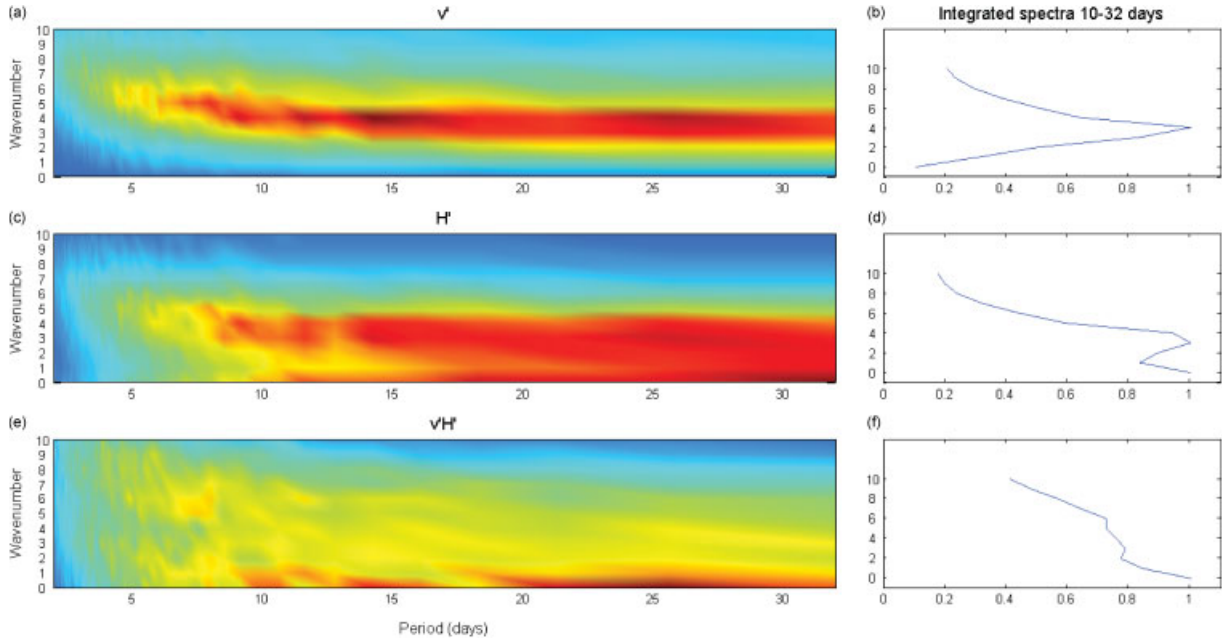

Figure 8. Same as Figure 7, but for SH JJAs from June 1989–August 2010. This figure is available in colour online at wileyonlinelibrary.com/journal/qj

4. Discussion

According to both physical (see MC13) and purely mathematical considerations (such as the bandwidth theorem), the observed extremes in $v'H'$ could plausibly be solely due to baroclinic disturbances. Traditional measures find that these time-scales and motions with periods longer than 10 days typically account for comparable portions of the 850 mb NH transient-eddy heat transport (Blackmon *et al.*, 1977). Intuitively, extremes must correspond to growing systems, which are associated with baroclinic perturbations. Therefore, when focusing specifically on extremes, one would expect the contribution of baroclinic scales to be significantly higher than normal. The present study finds that this is not the case: the v' and H' power spectra are found to peak at long periods and, as discussed above, these long periods provide the greatest contribution to the power in the $v'H'$ spectrum. Even though the coherence and phase characteristics of the v' and H' signals favour short-period fluctuations, this is not enough for the latter to account for the majority of the power in the $v'H'$ spectrum (see Table 1). It should also be noted that, as mentioned in section 3.1, periods beyond the baroclinic range in v' and H' can contribute to baroclinic motions in the $v'H'$ spectrum. Regardless of hemisphere and season, v' and H' fluctuations therefore combine to produce phase- and coherence-driven extreme events in heat transport which, as discussed in detail in MC13, account for over half of the poleward heat transport by transient eddies.

It should be noted that there are alternatives to the Eady-type wave view presented here, such as that suggested by Larichev and Held (1995). In the latter model, heat flux (or, more precisely, potential vorticity flux in the two-layer model framework) is dominated by the largest eddies excited by the inverse barotropic energy cascade, rather than by the deformation-scale ones. In this perspective, the low wave-number systems discussed in section 3.4

would be interpreted as equivalent barotropic waves, such as the annular modes. Note that, while in the net equivalent barotropic modes account for no heat transport, they can drive strong local fluxes. A caveat of this interpretation is that it is unlikely to apply to the SH, where the high coherence values discussed in Section 3.3 are more reminiscent of a linear wave regime.

Yet a different perspective is provided by the Heton model (Hogg and Stommel, 1985a, 1985b). Here, the wave view is abandoned altogether in favour of a particle approach, where heat transport is effected by pairs of point baroclinic vortices, termed Hetons. Since heat transport extremes are due to a complex interplay of different frequencies and wave numbers, it can be instructive to consider, instead, the interactions between point vortices. Indeed, a particle framework relates more intuitively to the concept of sporadic heat transport than the wave picture. Once could, for example, speculate that extreme events are the result of a cluster of Hetons travelling together.

All these considerations do not exclude a direct correspondence between extreme heat transport events and atmospheric mesoscale features. To this end, the authors are currently investigating the spatial features of the extremes. Even though a full discussion of said features is beyond the scope of the present study, it is interesting to note the effects they might have on the transport wavelet spectra. A striking result is the asymmetry in the zonal structure of the extreme events, with the poleward heat transport systematically tilting westwards with height. In the context of large-scale eastward advection during the NH winter months (DJF), one would expect to see this zonal asymmetry mirrored in the wavelet spectrum, as is indeed the case in Figure 1(e). The marked asymmetry in the power spectrum is not seen during SH JJA (see Figure 2(e)).

One of the strongest candidates for mesoscale signatures of extreme heat transport events would be the warm conveyor belts (WCBs) associated with extratropical cyclones. WCBs are streams of moist, rapidly ascending air parcels which rise from the boundary layer into the upper troposphere. Both their typical duration of a few days and their sporadic occurrence are consistent with the characteristics of the extreme events (Eckhardt *et al.*, 2004). Furthermore, there is no immediate reason that the wave-packet picture suggested in the Introduction should be inconsistent with the WCBs. A comparison of a climatology of extreme heat transport events from MC13 and one of WCBs from Eckhardt *et al.* (2004, their figure 3(b) and (f)), however, highlights noticeably different geographical distributions. Admittedly, the two climatologies cover non-overlapping periods (1993–2005 versus 1979–1993), but this is unlikely to explain the very different distributions displayed. As noted in MC13, the pattern of heat transport extremes in NH DJF is characterised by numerous areas of high activity: the Atlantic and Pacific storm tracks, the lee of the Rocky Mountains, the Bering Strait and the Nordic Seas. Only two of these maxima, namely the storm tracks, are also regions of high WCB activity. Similar discrepancies are seen in the JJA season. In the SH, the patterns are broadly similar in DJF, with both climatologies displaying a continuous band of activity around the Southern Ocean. During JJA, however, the band of high extreme event frequency occurs significantly further south than the WCBs. The profound differences found suggest that, even though WCBs could be associated with extreme heat-transport days in some regions of the globe, they are unlikely to drive the majority of these events. This is in agreement with the results discussed in section 3.4, which imply that there might be no direct mesoscale or synoptic analogues for the extremes.

5. Conclusions

The present article focuses on wavelet spectral analysis of extreme events in meridional transient eddy heat transport. The analysis is in terms of v', H' and $v'H'$ power spectra and v' and H' cross-power and coherence-phase plots. The outstanding feature of the v' and H' spectra is their increase in power with increasing period, a feature that is not reproduced in the $v'H'$ spectra. As a result of these features, baroclinic time-scales in v' and H' fluctuations account for a limited part of the power in the extreme $v'H'$ days, comparable to that seen for average transport days. It is also found that power at periods beyond the baroclinic time-scales is mainly driven by planetary-scale waves, suggesting that the extreme events do not necessarily have a precise synoptic analogue.

As discussed in the Introduction, the importance of the longer periods is not obvious from a simple evaluation of the bandwidth theorem. However, the theorem only sets a lower bound on the required range of frequencies. Indeed, wave packets are commonly expressed as an integral over an infinite spread of wave numbers (and hence angular frequencies). Analogously to this, the present study therefore finds that the localized extreme occurrences in $v'H'$ require a much broader range of frequencies than the lower limit set by the bandwidth theorem. This counters the naïve expectation of a strong link between extreme transport events and growing baroclinic systems and highlights the roles of phase and coherence, across a broad range of frequencies, in generating extreme $v'H'$ occurrences.

The importance of phase in generating extremes had already been hypothesized in MC13, in the context of baroclinic time-scales. Here, the result is established robustly and placed in the context of the time–frequency characteristics of the spectra. Furthermore, the role of coherence is added to the picture. Indeed, it is shown that the key to generating an extreme lies in the coincidence of ideal coherence and phase relationships and that only one of the two is a necessary but not sufficient condition. An important consequence of this finding is that extreme event days might not be immediately distinguishable from random days in terms of v' and H' spectral characteristics, meaning that, potentially, moderate v' and H' anomalies at periods beyond baroclinic time-scales could drive very large meridional transport events.

Acknowledgements

G. Messori is funded by a bursary from the National Environment Research Council (RAPID–RAPIT project). ERA-Interim reanalysis data were obtained from the BADC ftp server at ftp.badc.rl.ac.uk. The wavelet software was provided by C. Torrence and G. Compo, available at http://atoc.colorado.edu/research/wavelets/, and by A. Grinsted, J.C. Moore and S. Jevrejeva, available at: http://noc.ac.uk/using-science/crosswavelet-wavelet-coherence. Discussions with M. O. Archer were of great help for performing the wavelet analysis. We also thank the two anonymous reviewers for their insightful feedback.

References

Blackmon ML, Lau N-C. 1980. Regional characteristics of the Northern Hemisphere Wintertime circulation: a comparison of the simulation of a GFDL general circulation model with observations. *J. Atmos. Sci.* **37**: 497–514.

Blackmon ML, Wallace JM, Lau N-C, Mullen SL. 1977. An observational study of the Northern Hemsiphere Wintertime circulation. *J. Atmos. Sci.* **34**: 1040–1053.

Branscome LE. 1983. A parameterization of transient eddy heat flux on a beta-plane. *J. Atmos. Sci.* **40**: 2508–2521.

Carleton AM. 1988. Meridional transport of eddy sensible heat in winters marked by extremes of the North Atlantic Oscillation, 1948/49–1979/80. *J. Climate* **1**: 212–223.
Chang EKM. 1993. Downstream development of baroclinic waves as inferred from regression analysis. *J. Atmos. Sci.* **50**: 2038–2053.
Eady ET. 1949. Long waves and cyclone waves. *Tellus* **1**: 33–52.
Eckhardt S, Stohl A, Wernli H, James P, Forster C, Spichtinger N. 2004. A 15-year climatology of warm conveyor belts. *J. Climate* **17**: 218–237.
Goupillaud P, Grossmann A, Morlet J. 1984. Cycle – octave and related transforms in seismic signal analysis. *Geoexploration* **23**: 85–102.
Grinsted R, Moore JC, Jevrejeva S. 2004. Applications of the cross wavelet transform and wavelet coherence to geophysical time series. *Nonlin. Process. Geophys.* **11**: 561–566.
Hamilton K. 1983. Aspects of wave behaviour in the mid- and upper troposphere of the southern Hemisphere. *Atmos. Ocean* **21**: 40–54.
Hogg NG, Stommel HM. 1985a.. The heton, an elementary interaction between discrete baroclinic geostrophic vortices, and its implications concerning eddy heat-flow. *Proc. R. Soc. London, Ser. A* **397**: 1–20.
Hogg NG, Stommel HM. 1985b.. Hetonic explosions: the breakup and spread of warm pools as explained by baroclinic point vortices. *J. Atmos. Sci.* **42**: 1465–1476.
Larichev VD, Held IM. 1995. Eddy amplitudes and fluxes in a homogeneous model of fully developed baroclinic instability. *J. Phys. Oceanogr.* **25**: 2285–2297.
Lau N-C, Wallace JM. 1979. On the distribution of horizontal transports by transient eddies in the Northern Hemisphere wintertime circulation. *J. Atmos. Sci.* **36**: 1844–1861.
Messori G, Czaja A. 2013. On the sporadic nature of meridional heat transport by transient eddies. *Q. J. R. Meteorol. Soc.* **139**: 999–1008.
Nakamura H, Izumi T, Sampe T. 2002. Interannual and decadal modulations recently observed in the Pacific storm track activity and East Asian Winter Monsoon. *J. Climate* **15**: 1855–1874.
Peixoto JP, Oort AH. 1992. *Physics of Climate.* American Institute of Physics: New York, NY.
Simmons A, Uppala S, Dee D, Kobayashi S. 2006. ERA-Interim: New ECMWF reanalysis products from 1989 onwards. *ECMWF Newsletter* **110**: 25–35.
Swanson KL, Pierrehumbert RT. 1997. Lower-tropospheric heat transport in the Pacific storm track. *J. Atmos. Sci.* **54**: 1533–1543.
Torrence P, Compo GP. 1998. A practical guide to wavelet analysis. *Bull. Am. Meteorol. Soc.* **79**: 61–78.

